MNRAS **000**, 1–11 (2018) Preprint 17 January 2019 Compiled using MNRAS LATEX style file v3.0

A high-resolution view of the jets in 3C465

E. Bempong-Manful[1,2⋆], M.J. Hardcastle[1], M. Birkinshaw[2] and the e-MERLIN Legacy jet project
[1]*School of Physics, Astronomy and Mathematics, University of Hertfordshire, College Lane, Hatfield AL10 9AB, UK*
[2]*School of Physics, University of Bristol, Tyndall Avenue, Bristol BS8 1TL, UK*

Accepted XXX. Received YYY; in original form ZZZ

ABSTRACT
We present new high-resolution and high-sensitivity studies of the jets in the WAT source 3C465, using deep transverse resolved radio observations from e-MERLIN, and with complementary observations from the VLA. A detailed description of our radio maps is presented. We derive lower and upper limit values of $0.5c$ and 61° respectively for the jet velocity, β_j and angle to the line of sight, θ. Our spectral analysis shows that the jet spectrum is fairly constant ($<\alpha_{jet}> = -0.7$), and that the observed spectral flattening within the first 4.4 kpc radius from the core coincides with the region hosting the bright knots, and is consistent with the site of X-ray particle acceleration observed at the base of the radio jet in previous studies. There is very little dispersion ($<\Delta\alpha> = -0.04$) between the spectra of the two hotspot components, plausibly indicating that electron populations of the same properties are injected at these sites. The NW and SE plumes are approximately homologous structures, with variations in mass injection and propagation in external pressure and density gradients in the two regions plausibly accounting for the comparatively steeper spectrum in the NW plume, $<\alpha_{NWp}> = -1.43$ compared with the SE plume, $<\alpha_{SEp}> = -1.38$. Overall, our results show that first-order Fermi process at mildly relativistic shocks is the most likely acceleration mechanism at play in 3C465; and consistent with previous works, we conclude that two plausible acceleration mechanisms; (a) when bulk flow speeds, $\beta_j \geq 0.5$, and (b) when flow speeds, β_j are less than ≈ 0.5 exist in our radio sample. Whereas the first case can accelerate electrons to high Lorentz factors, the second scenario dominates at slower speeds and larger distances.

Key words: galaxies: active – galaxies: jets: particle acceleration.

1 INTRODUCTION

Relativistic plasma ejected from SMBHs at the centres of massive galaxies is known to play a key role in the AGN feedback cycle, and consequently the formation and evolution of structure in the universe. The formation, collimation and acceleration of these cosmic outflows is of ongoing importance in the field of astrophysical research, and notwithstanding the vast range of physical systems from which they are produced, cosmic jets and outflows are thought to be driven by essentially similar physical mechanisms (e.g. Wiita 2001). In the case of a supersonic jet beam, dynamical instabilities associated with these outflows are rich enough to allow the formation of structures such as knots, filaments and wiggles (e.g. Stone 1997) and these have been observationally confirmed and studied in detail (e.g. Hardcastle et al. 2002; Laing et al. 2006).

In spite of the complex morphologies exhibited by extragalactic radio sources, both type I and II of the Fanaroff and Riley (Fanaroff & Riley 1974) morphological classification of radio-loud AGNs to a certain extent, tend to have pairs of jets in the plane of the sky (e.g. Urry & Padovani 1995). The FR Is are relatively low-power radio sources with twin jets that are initially relativistic on parsec scales, but decelerate from relativistic to sub-relativistic speeds on kpc scales. The jets exhibit considerable brightness asymmetry at their base (e.g. Parma et al. 1996), are thought to be transonic (i.e., no strong shocks are observed at their termination points) on kpc-scale velocities, and are both easily observed on large scales due to the absence of strong Doppler boosting effects (e.g. Worrall et al. 2007). Laing (1993) also notes that the orientation of the magnetic field configuration relative to the jets in these sources changes from longitudinal to transverse as the jet propagates.

Wide-angle tailed (WAT) radio galaxies, generally classified as FR I sources, are associated with central cluster galaxies (e.g. Owen & Rudnick 1976) and have luminosities at the FR I/FR II break. They exhibit one or twin well-collimated jets which usually extend for tens of kpc before flaring into their characteristic plumes at their termination point, and the jets have polarisation structures that closely resemble those of FR II sources (e.g. Hardcastle & Sakelliou 2004). Although they form a relatively small minority of

⋆ E-mail: e.bempong-manful@bristol.ac.uk (EBM)

Table 1. Summary of observations

Band (GHz)	VLA observations				e-MERLIN observations			
	A-configuration		B-configuration		Epoch-1		Epoch-2	
	Date	Time(h)	Date	Time(h)	Date	Time(h)	Date	Time(h)
L (∼1.5)	31 Oct 2012	1.2	28 May 2012	1.2	12 Apr 2015	19.0	13 Apr 2015	19.3

the radio source population, the bending of the tails – the feature that distinguish it from typical twin-jet FR Is and gave the class its name – has long been the subject of interest (e.g. Eilek et al. 1984). Indeed numerous theories including electrodynamic effects; Bodo et al. (1985); gravitational bending; Burns et al. (1982); buoyancy effects; Worrall et al. (1995) and ram pressure; Venkatesan et al. (1994) have been proposed in the literature to account for tail-bending in radio galaxies. However, WATs with their characteristic luminosities near the FR I/FR II break (e.g. Hardcastle & Sakelliou 2004), varied bending angles (i.e., 30 – 115 degrees) (e.g. O'Donoghue et al. 1993) and collimated jets which often travel several kpc into the ICM before flaring into plumes, present an unusual challenge. Earlier work by Hardcastle & Sakelliou (2004) in a study of selected WATs in Abell clusters of galaxies suggests that the jets in WATs terminate in a variety of ways, further underscoring the complexity of the physical mechanism that initiates the bending in these class of radio sources.

3C465 is associated with NGC7720, the dominating "diffuse" galaxy in the cluster Abell 2634, and is among the best studied WAT sources in the northern sky due to its proximity and peculiar morphology within this class of radio sources. Detailed imaging studies in the optical (e.g. Colina & Perez-Fournon 1990; Capetti et al. 2005), radio (e.g. Leahy 1984; Hardcastle & Sakelliou 2004) and X-ray (e.g. Schindler & Prieto 1997; Hardcastle et al. 2005) observations of the source have previously been made. Its jet and hotspots as shown in our total intensity maps (see Section 3.2) have been extensively studied and large-scale properties of the plumes are also well known. The tails of WAT sources generally bend in a common direction, resulting in their overall characteristic U, V, or C shape. These sources are generally assumed to form by motion of the host galaxy relative to the cluster: the host galaxies are thought to be nearly stationary at the bottom of cluster potential wells, moving with velocities $\sim$ 200 km s^{-1} in an oscillatory motion of small amplitude ($<$ 0.3 of a core radius) (e.g. Burns et al. 1982).

Although driven by essentially similar underlying physical mechanisms, the morphology, kinematics and dynamics of these jets is heavily subject to differences in host galaxy properties and environment, and efforts are ongoing to constrain the physics driving the observed jet structure in these cosmic outflows, including where and how particles are accelerated in the jets and hotspots, among other questions. As part of the e-MERLIN Legacy project, which aims to resolve some of these key questions in extragalactic jet physics, we present new high-resolution and high-sensitivity studies from multi-configuration, multi-frequency VLA and e-MERLIN observations of the WAT source 3C465.

Throughout this paper, we assume a concordance cosmology with Ω_m = 0.27, Ω_Λ = 0.73, and H_0 = 75 km s^{-1} Mpc^{-1}. At the current best known redshift of 3C465 (i.e., z = 0.029), one arcsec is equivalent to a projected length of 0.56 kpc. Spectral indices, α are defined in the sense $S \propto \nu^{\alpha}$. J2000 co-ordinates are used throughout.

2 DATA AND METHODS

2.1 Observations, calibration and imaging

3C465 was observed with both the expanded VLA and e-MERLIN at L-band continuum frequencies centred on 1.5 GHz using a bandwidth of 512 MHz. Observations at this frequency and in particular the two VLA configurations (see Table 1) were undertaken in view of the scientific objectives of the present study – that is, the e-MERLIN array with its long baselines yielded higher angular resolution of the science target, whereas the more diffuse large scale structure were contributed by the shorter baselines of the VLA to deliver the best possible instantaneous *uv* coverage, which is essential to constructing high fidelity images. The data were calibrated and imaged using the standard procedure in CASA and AIPS respectively for the VLA and e-MERLIN datasets. As a standard technique in all VLBI observations, we performed fringe-fitting on the e-MERLIN datasets prior to calibration. The X-Band ($\sim$ 8.5 GHz) VLA data used in the present analysis is the data of Hardcastle & Sakelliou (2004) and was observed in all four configurations (A, B, C and D) of the VLA with bandwidths of 25 MHz (for the A-configuration observations) and 50 MHz (for the rest).

2.2 Data combination and mapping

Data combination from very different interferometry elements – as is the case in the present study – can be relatively problematic due to fundamental differences in the structure of the visibilities from the different arrays. Although the combination can be achieved in the sky-plane or the *uv* plane, we have carried out the combination in the Fourier plane to allow for better constraints on the CLEAN algorithm (see Biggs & Ivison 2008).

We calibrated and imaged separately the A and B-configurations of the VLA datasets before combining the two configurations into a single measurement set. A similar approach was used for the two e-MERLIN observing epochs to account for baselines that included the Lovell telescope and the non-Lovell baseline. The resulting datasets from the two interferometry elements were then used to create a complete e-MERLIN/VLA dataset, but this time with appropriate weighting scales for the two array visibilities to account for differences in the weighting schemes for the two arrays. Finding the optimum weighting factor requires some form of verification by visual inspection, and in the present study we varied the weights and formed the dirty beam using *wsclean* (see Offringa et al. 2014) to try to find the point where the baselines of the combined dataset were not dominated by that of the VLA. Such comparable statistical weightings were obtained with approximate factor of:

$$\frac{W_{VLA}}{W_{eMERLIN}} = \frac{3 \times 10^{-7}}{1} \quad (1)$$

This allowed us to construct total intensity maps of the combined dataset with a beam size approximately equal to the e-MERLIN –

Table 2. Properties of radio maps presented

Map	Restoring beam			Core flux	Off-source	RA (J2000)	DEC (J2000)	Figure
	Major axis (arcsec)	Minor axis (arcsec)	Pos. angle (°)	density(Jy)	noise(μJy)			label
VLA^L	1.37	1.13	71.02	0.21	34.64	23 38 29.39	+27 01 53.53	a
e-MERLIN^L	0.27	0.15	19.26	0.21	31.05	23 38 29.39	+27 01 53.53	b,c,d
e-MERLIN^L+VLA^L	0.39	0.37	108.24	0.71	33.66	23 38 29.39	+27 01 53.53	f
VLA^L	1.5	1.5	0.00	0.21	34.92	23 38 29.39	+27 01 53.53	NS
VLA^X	1.5	1.5	0.00	0.21	20.22	23 38 29.39	+27 01 53.53	NS
VLA^X	0.5	0.5	0.00	0.21	22.75	23 38 29.39	+27 01 53.53	NS
e-MERLIN^L+VLA^L	0.5	0.5	0.00	0.19	31.43	23 38 29.39	+27 01 53.53	NS

Notes: The superscripts L and X respectively denote $\sim$ 1.5 GHz and $\sim$ 8.5 GHz observing frequency used in our present study. The VLA L-band data was observed in A and B configurations whereas the X-band data was observed in A,B,C and D configurations. Maps not shown in the text are denoted NS in the figure label column.

only beam ($\sim$ 150 mas). Deconvolution of the e-MERLIN/VLA dataset was executed in *wsclean* with the *Briggs weighting* scheme – with *Briggs* robustness parameter set to -1.5 to give further weighting to the longer baselines contributed by the e-MERLIN visibilities.

2.3 Resolution matching

Our combined e-MERLIN/VLA map (hereafter referred to as the 1.5 GHz map) has a resolution of $\sim 0.39 \times 0.31$ arcsec. It would have been possible to obtain a beam size approximately equal to the e-MERLIN only beam size. However, it is impossible to obtain good image fidelity of the 8.5 GHz map at such high spatial resolutions. For accurate determination of spectral indices across the two frequencies, we needed to convolve the 1.5 and 8.5 GHz maps to equivalent resolutions (i.e., 0.5 and 1.5-arcsec). This was necessary to ensure that any recovered flux at both frequencies included emission extended on scales up to those consistent with the 8.5 GHz restoring beam. This allowed us to effectively measure flux densities from the same spatial region from each map. At higher resolutions we are less sensitive to extended emission of the source and vice versa, and this has been accounted for in our estimates of the spectral indices – with the 0.5-arcsec resolution map used for the jet and hotspot regions while the 1.5-arcsec resolution map has been used for the plumes. We have performed primary beam correction on the 8.5 GHz map. This allows us to measure precise flux densities and corresponding errors since the shortest baselines sampled by the two maps are similar – so that we are sensitive to the same extended structure (plumes) across the two frequencies.

3 THE WAT SOURCE 3C465

3.1 The radio core

A few percent of mJy radio sources are known to exhibit variability on timescale of years (e.g. Oort & Windhorst 1985). However, there was no observed variability of the radio core of 3C465 over the timescales of the VLA observations at 1.5 or 8.5 GHz and/or e-MERLIN observations at 1.5 GHz, within the errors imposed by the uncertainty of absolute flux calibration at either the VLA or e-MERLIN array. Its flux density measured from the two interferometry elements (and in the case of the VLA, the two configurations deployed in our observations) is reported in Table 2. The best position for the core is RA 23h38m29.39s, Dec 27°01′53.″25.

3.2 Jets, knots, hotspots and plumes

Our low-resolution map (Fig. 2(a)) show the peaked central emission and the elongation of the overall radio structure in the NW-SE direction, consistent with the characteristic U or C-shaped morphology exhibited by these class of radio sources due to ram pressure arising from bulk motion of the host galaxy relative to the cluster. The total angular extent of 3C465 estimated from our $\sim 1.37 \times 1.13$ arcsec resolution 1.5 GHz VLA map is 7.60 arcmin. This corresponds to a projected angular size of 456 arcsec ($\sim$ 275 kpc) – about a factor 1.3 lower than that measured by Leahy et al. (1996) at similar frequency but different configurations (A & C) of the VLA. Sensitivity to extended structures at C-configuration of the VLA is comparatively higher than B-configuration at similar frequencies and this accounts for the difference in our observed angular size of the radio source. Our radio image shows two very narrow, well collimated jets (denoted NW and SE) emanating from the core of the galaxy, with the jet that is presumably pointing towards us (NW jet) exhibiting considerably higher surface brightness over almost its full length compared with the counterjet (SE jet). Our e-MERLIN only image (Fig. 2(b)) represent the highest resolution *deep transverse resolved radio observation* map of 3C465 to date, and with the short baseline contribution from the VLA in our combined e-MERLIN/VLA map (Fig. 2(f)) we can further construct the highest resolution and sensitivity map of the source. In our high resolution map (Fig. 2(b)), the counterjet is not visible and the jet is seen as a one-sided jet – a feature which 3C465 shares in common with classical double (FR II) radio sources.

The NW jet is well resolved and has a cross-sectional width of $\sim$ 0.32 arcsec measured over the inner region where the jets are bright and straight. At high resolution, there is clear evidence of a knotty structure at the base of the NW jet of 3C465 – a feature observed earlier by Hardcastle & Sakelliou (2004). However at e-MERLIN resolution (see Fig. 2(d)) our good image fidelity allows us to infer multiple bright knotty structures – two of which are visible at the very edge of the core, the very point where the jet is first seen emanating from the central engine, and a third knot which lies between the two knots denoted NJ1 by Hardcastle & Sakelliou (2004). Beyond 4.4 kpc from the inner jet, there is no clear evidence of such knotty structures of intense radio emission until the main site of energy dissipation in the bright compact region (hotspot) denoted NW hotspot near the base of the NW plume (Fig. 2(f)).

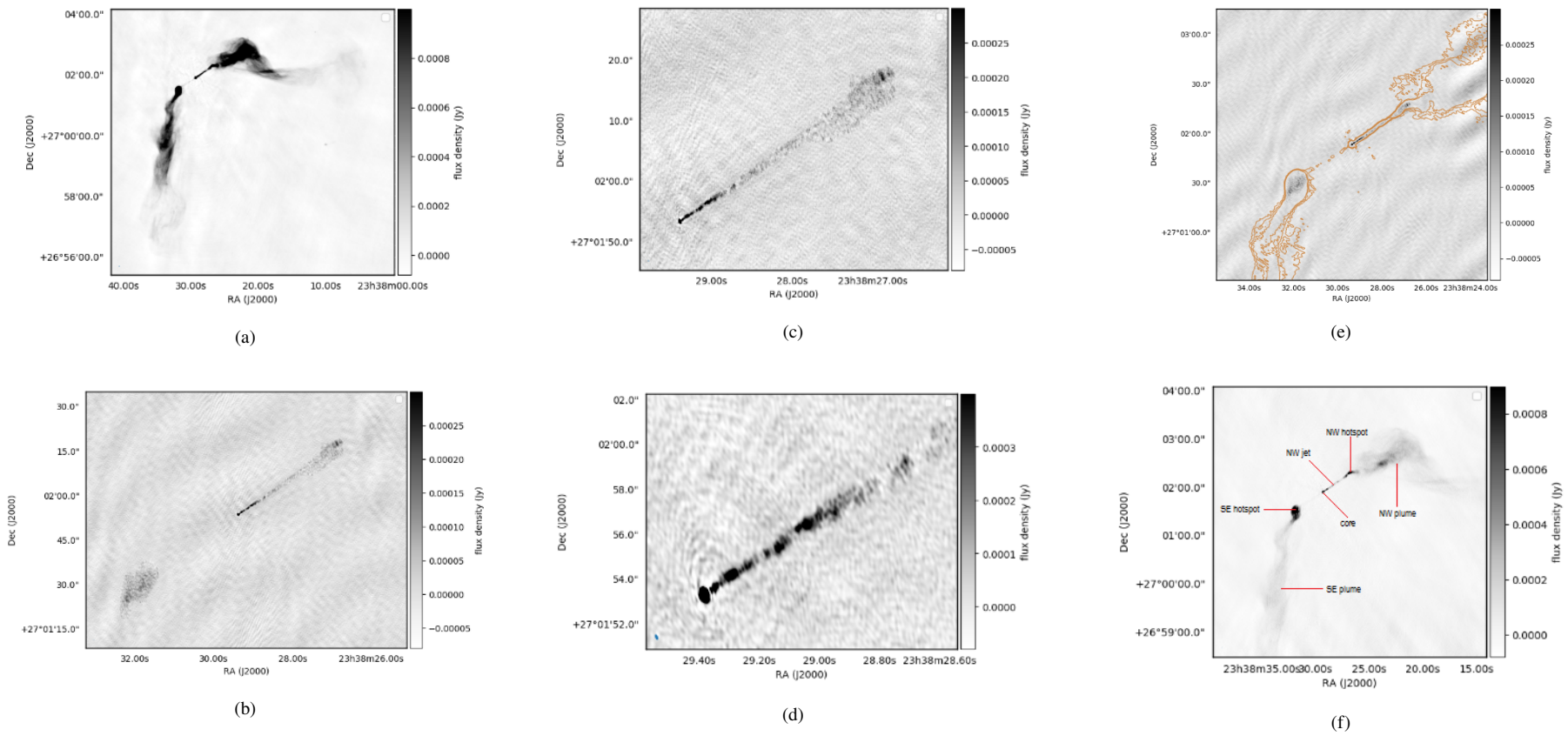

Figure 2. L-Band (∼1.5 GHz) radio maps of the WAT source 3C465. (a) A+B–configuration VLA map at 1.37×1.13-arcsec resolution; (b) e-MERLIN map at 0.27×0.15-arcsec resolution (note the sidedness of the radio jet); (c) & (d) 0.27×0.15-arcsec e-MERLIN maps showing the jet only region and zoom in on the inner 5 kpc radius from the core respectively (note the visible bright knotty structures at the jet base and the elliptical shape of the recovered primary beam); (e) e-MERLIN map with superposed VLA contours (grey scale) showing the jet and hotspots, and parts of the extended structures (plumes); (f) combined e-MERLIN plus VLA map at 0.39×0.37-arcsec resolution (note the continued collimated outflow from the NW hotspot into the base of the NW plume).

This hotspot is at $\sim$ 23.4 kpc projected from the core and corresponds to the termination point of the NW jet. The SE hotspot exhibits a relatively broad bright structure compared with the NW hotspot. Since both jets must carry power of equal magnitude (for momentum conservation), it is difficult to assign a physical interpretation to this striking asymmetry between the two hotspot regions – which appears characteristic of this class of radio galaxies [see Hardcastle & Sakelliou (2004) for similar asymmetry in a sample of 7 WAT sources including 3C465]. A plausible explanation however could be the degree of jet-environment interactions at the two sites – with what appears to be a "mini" overpressured cocoon at the SE hotspot region resulting from a relatively higher density environment in pressure equilibrium with the ICM.

From the termination point of the NW jet ($\sim$ 29.8 kpc in projection), the NW plume is observed to extend in the jet direction (northwestwards). However, after a distance of $\sim$ 39.1 kpc from its base, the rapid change in direction is particularly obvious. There are two pronounced bends, at almost 90° – first, southwestwards and then westwards, and the jet appears to bend once more in the northwest direction at $\sim$ 90° towards the tail end of the NW plume to form a bell shape. Within the limitations of sensitivity to large-scale structures in our observations, we suggest that this bending trajectory (northwest – southwest – northwest) implied by the NW plume could be episodic, stretching over several tens – hundreds of kpc into the IGM. The rather striking feature here is the apparent asymmetry in morphology of the two plumes. Unlike the NW plume, the SE plume shows no prominent bends except for a wiggled pattern downstream. Since the plumes in WAT sources are generally thought to be analogous to smoke from factory chimneys (i.e., light slow-moving structures strongly affected by bulk motions in their environments), these wiggles are likely the result of strong interaction between the large-scale flow within the plume (which must be light compared with the external medium) and features of the external environment due to either thermal or ram pressure. We attribute the observed asymmetry in physical size and structure of these two large scale components to 2-D projection effects such that the SE plume if projected in a different direction could exhibit similar prominent bends as the NW plume. The radio source fades into the noise on these images and, as noted above, the source is likely to be more extended than the estimated angular size quoted in our present analysis.

3.3 Jet speed and sidedness ratio

The good image fidelity of our maps allows us to estimate the jet/counterjet ratio in our sample and place constraints on the jet speed and angle to the line of sight in 3C465. Following the procedure defined by Hardcastle et al. (1998), and using our 1.5 GHz VLA map at 1.5-arcsec resolution, we measured only the straight part of the jet and counterjet, over equivalent angular extent – to avoid any discrepancy in the angle it makes with the line of sight over the integration region. We measure flux densities of 60.16 $\pm$ 0.66 mJy and 4.05 $\pm$ 0.14 mJy for the jet and counterjet respectively, and obtain a sidedness ratio of 14.85 $\pm$ 0.80. Our estimated sidedness ratio is approximately a factor 3 higher than that obtained by Hardcastle & Sakelliou (2004) for this WAT jet at 8.5 GHz, and is probably a better estimate due to the improved bandwidth capabilities of the new VLA deployed in our observations. We again assume that the jets are intrinsically symmetrical and that the observed jet flux asymmetries are due to relativistic beaming effects. This allow us to constrain the characteristic beaming speed, β_j and angle it makes with our line of sight, θ by defining the ratio of the jet and counterjet flux densities, $J_\nu = S_j/S_{cj}$ as:

$$J_\nu = \left(\frac{1+\beta_j \cos\theta}{1-\beta_j \cos\theta}\right)^{\delta} \tag{2}$$

where, $\beta_j c$ is the speed of the jet, which is inclined at an angle, $\theta \in [0, \pi/2]$ to our line of sight, and $\delta = \mathrm{m} + \alpha$; the constant m = 2 for a continuous jet (see Scheuer & Readhead 1979 for review). α is the spectral index, which is taken to be 0.6.

The observed jet/counterjet asymmetry favours relativistic speeds in the jet – at least in the regions close to the inner core. From our analysis, we find that $\beta_j \cos\theta = 0.48$. Since a lower limit on $\cos\theta$ corresponds to an upper limit on θ, we obtain lower and upper limit values of 0.5 and 61° for β_j and θ respectively. We find our estimated jet speed, $v_j \geq 0.5c$ to be consistent with the range of values (0.3 – 0.7)c obtained by Jetha et al. (2006) in their study of jet speeds in a sample of 30 WAT radio galaxies including 3C465.

4 SPECTRAL ANALYSIS AND RESULTS

4.1 Spectral-index estimates and mapping

Since our data cover only two frequencies, we have directly calculated the spectral indices as: $\alpha_{\nu_1}^{\nu_2} = [S(\nu_1)/S(\nu_2)]\ln(\nu_1/\nu_2)$, by constructing polygonal regions for flux density measurements within the convolved equivalent maps. Where necessary we used polygons slightly wider than regions of *real* emission to reduce sensitivity to any residual misalignments between the maps. Background was taken from the rms errors in total intensity I from circle of radius 10.96 arcsec fixed in position. Since the rms error just depends on the ratio ν_1/ν_2, by standard error propagation we can estimate fractional errors in α across the two frequencies as:

$$\sigma_\alpha = \frac{\sigma_I}{R} \Big/ \ln\left(\frac{\nu_1}{\nu_2}\right) \tag{3}$$

where σ_I is the fractional error on the ratio of the two flux densities and R is the ratio of the two flux densities itself – the error of which depends on the error (noise levels) on the maps, and ν_1 and ν_2 are frequencies corresponding to the L-Band ($\sim$ 1.5 GHz) and X-Band ($\sim$ 8.5 GHz) respectively used in our present analysis.

We emphasize that this is a relatively crude model in estimating the error on individual flux density values across the two frequencies. However if we adopt a similar noise level over different regions of flux density integration in our maps and assume that errors in I have a Gaussian distribution with zero mean and rms σ_I in the image plane and that they are independent on scales larger than the primary beam, then our errors should be robust. For consistency, spectral indices at the two resolutions were independently examined at the hotspot region, and this yielded values of -0.73 ± 0.01 and -0.75 ± 0.01 for the 0.5"(1.5") resolution respectively, showing that the two sets of maps are consistent. In constructing our spectral-index map we took background to be the off-source noise level σ_{off} in I and created the map at 3σ cut-off at this rms value over the two frequencies. Finally, due to the complex structure of our source, we have carefully estimated our distances taking into consideration the trajectory of the radio jet to account for the bending of the tail of the radio source through the IGM. All flux profile axes in our plots are logarithmic scales and except where explicitly stated, all distances are with respect to the central unresolved feature, coincident with the nucleus (core) of the host galaxy.

Figure 3. Map of spectral index, α of the WAT radio source 3C465 constructed from maps made at two frequencies ($\sim$ 1.5 and $\sim$ 8.5 GHz) at 1.5–arcsec resolution. α is in the range –0.5 to –0.8 and –1.1 to –2.3 over the jet and plume regions respectively and is plotted at 3σ rms noise cut-off in total intensity.

4.2 Flux density and spectral index map, distribution and properties

We observed a correlation in the flux density distributions measured over the two frequencies along the jet, hotspots and plumes of our radio sample (see Fig. 4, 6, 7). Figure 3 above shows a grey-scale image of the spectral index over the range –0.3 $\leq \alpha \leq$ –2.3 for 3C465. With the exception of the unresolved core, which is partially optically thick with $\alpha \sim$ –0.4, the emission typically has –0.5 $\leq \alpha \leq$ –0.8 over the jet region and –1.1 $\leq \alpha \leq$ –2.3 in the plumes. It is noteworthy that close to the edges of the jet, small errors in deconvolution can cause significant changes in α (i.e., high or low spectral index values), and this is also true for regions where signal-to-noise ratio is low. The mean spectral index of the jet and counterjet (estimated from our spectral index map) is –0.70 $\pm$ 0.04 and, as discussed in section 4.3.1, it shows a fairly constant spectrum. However, the overall spectral index profile of the plumes is observed to steepen rapidly with distance from the AGN. This spectral behaviour is as expected in the standard model in which the radio tails flow slowly away from the host galaxy and eventually become dominated by the presence of old electron population (radiative ageing) resulting in steeper spectra away from the core – compare the spectral index map of the WAT source 3C130 by Hardcastle (1998). Distributions of flux densities and corresponding spectral indices in the entire sample are plotted and discussed further in the sections to follow.

A distinctive feature of our spectral index map (see Fig. 3) is the long flat-spectrum filament which leaves the NW hotspot and extends in the jet direction (northwest) into the base of the NW plume, possibly suggesting some continued collimated outflow of plasma into the large-scale structures, and is observed to eventually terminate in a broad bright region in the NW plume. A similar observation has been made earlier in the WAT source 3C130 by Hardcastle (1998), and more recently by Hardcastle & Sakelliou (2004) in their study of selected WAT samples in the Abell clusters of galaxies. Although Hardcastle and Sakelliou did not directly observe our spectral index behaviour, they observed that the jets in some sources of their sample propagate without disruption for some distance into the plumes, and with such additional evidence we cautiously argue that this feature could well be a defining characteristic of these class of radio sources.

4.3 Spectral profiles

4.3.1 The jet and knots

At 0.5-arcsec resolution, the counterjet in our map is not bright enough to be imaged well and so our analysis here is limited to the NW jet of the source. Individual integrated spectral indices at locations chosen throughout the jet are plotted in Figure 4. These show a fairly constant spectral profile over almost the entire jet length, although there is some fractional steepening and flattening at a few discrete regions along the jet axis. Our estimate of $\sim$ 29.8 kpc for the jet length is approximately a factor 2 higher than the termination length of the jet in 3C465 reported by Hardcastle & Sakelliou (2004). This arises from our inclusion of the trajectory in measuring distances along the jet to account for the bends in the radio source. There are considerably high error bars on the spectra from $\sim$ 6–17 kpc; and noticeably so between $\sim$ 10–17 kpc inclusive. This stretch corresponds to regions of considerable low surface brightness of the radio jet as seen in our total intensity (0.5-arcsec) resolution map and therefore the errors are large.

The comparatively constant distribution of the spectral profile of the jet spans over $-0.5 \leq \alpha_{jet} \leq -0.8$ with an average value of $<\alpha_{jet}> = -0.70 \pm 0.04$, as expected from radio synchrotron. As shown in Figure 4, within the first 4.45 kpc of radius from the core, the 3 point region of interest (ROI) spectral indices are observed to flatten from -0.80 ± 0.02 to -0.64 ± 0.02 ($\Delta\alpha = -0.16$) and thereafter increase marginally to -0.68 ± 0.03 ($\Delta\alpha = -0.04$). The spectral flattening over this geometric area indicates the presence of high energetic (young) electron population; and provides evidence of ongoing particle acceleration at the jet base. This is consistent with the fact that X-ray evidence for particle acceleration is found at the base of the radio jet within the knotty structures (Hardcastle et al. 2005). The rather interesting observation here is that the region of flattest spectral index ($\alpha = -0.55 \pm 0.07$) at a distance of $\sim$ 13.7 kpc does not correspond to either of the bright knots at the jet base or the compact region of intense radio emission (hotspot) nor to any feature in the X-ray data. Beyond 13.7 kpc, there is systematic steepening of the spectra from -0.55 ± 0.07 to -0.73 ± 0.04 until the bright compact region (hotspot). The spectrum over this 3 point region of intense radio emission is almost constant, with lower and upper limits of -0.65 ± 0.02 (-0.68 ± 0.01) respectively, and $<\alpha>$ = -0.66 ± 0.01. We discuss spectra of the hotspots further in the next section.

4.3.2 The hotspots

Integrated spectral profiles over the two hotspot (NW and SE) regions separately and for the two combined are plotted in Figure 6. For reliability and purposes of direct comparison, we used a circle of diameter 16.05 arcsec as our extraction region centred on the two components (see Fig. 5) and estimated the hotspot spectra over this area. Due to the relatively smooth transition of the NW jet into the base of the NW plume, our estimate over this angular extent for

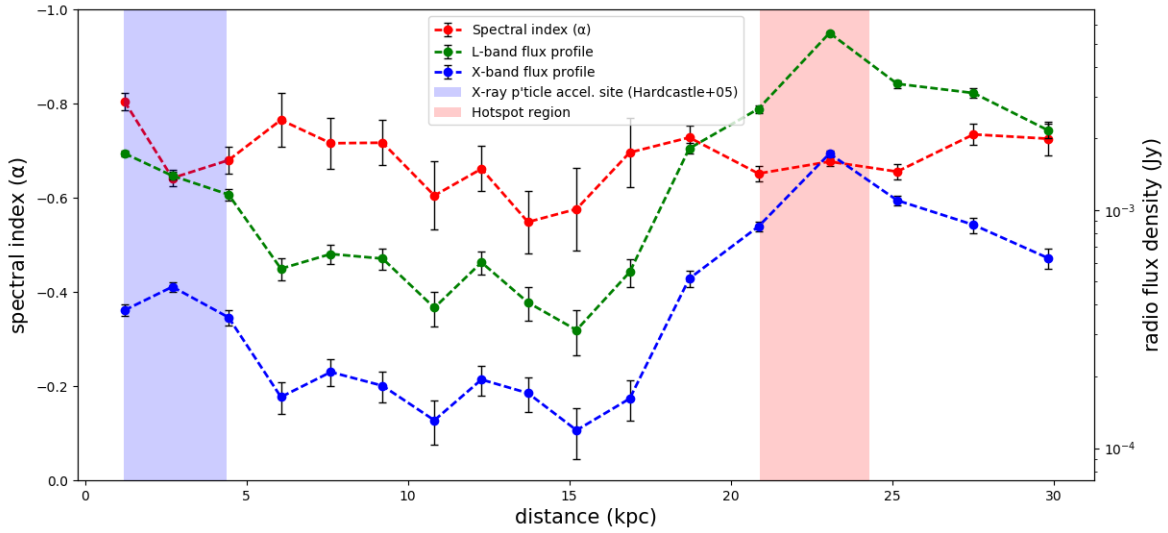

Figure 4. Profile of spectral index, α along the NW jet axis as a function of projected distance from the galaxy central region. Also shown are the respective flux density distributions measured at 1.5 and 8.5 GHz at a resolution of 0.5-arcsec. The error bars correspond to random errors σ_r from the rms errors in I only. Shown on the plot are also regions of interest (ROI) indicating site of X-ray particle acceleration as observed by Hardcastle et al. (2005) in a *Chandra* and *XMM-Newton* study of 3C465 – colour coded in blue tone; and the NW hotspot region – colour coded in red tone.

the NW hotspot region may be overestimated by a factor of a few in our present analysis and the opposite is true for the SE hotspot region which features a comparatively broad bright structure. The spectral indices over the integration regions in the hotspots show very little dispersion between the two components with mean values of $<\alpha_{NWh}> = -0.69 \pm 0.01$ and $<\alpha_{SEh}> = -0.65 \pm 0.01$ ($\Delta\alpha = -0.04$). This plausibly indicates that an electron population with the same properties is injected at these sites – consistent with the two components being at equal termination distances ($\sim$ 23.4 kpc) on either side of the host galaxy.

The NW hotspot spectrum (Fig. 6 (top pane)) exhibits considerable flattening within the first 2 kpc radius from the edge of the hotspot integration region. This shows a gradual decrease of α from -0.73 ± 0.01 to -0.61 ± 0.01 ($\Delta\alpha = -0.1$). Beyond this span, the spectrum steepens to -0.77 ± 0.01 and thereafter falls gradually to -0.62 ± 0.01 at $\sim$ 24.5 kpc, before experiencing a further upturn towards the end of the integration region. A slight but significant tendency for the spectral index to flatten over almost the entire SE hotspot geometric area is apparent from Figure 6 (middle pane), except for the final 3 points of integration at the tail end of the spectrum. The effect is subtle ($\Delta\alpha \leq -0.05$) nonetheless consistent; with a steady decline in α from -0.76 ± 0.01 to -0.57 ± 0.01 ($\Delta\alpha = -0.2$), plausibly indicating acceleration of high energy electrons as would be expected in the case of typical classical double (FR II) radio galaxies. Unlike the SE, there is no clear trend in NW hotspot spectra and except for the first integration point, the spectra for the NW hotspot is slightly broader than the SE at all our fiducial locations; this is expected from the larger random errors in the NW hotspot due to its comparatively narrower distribution.

Indeed from the standard model, if the spectrum is not a pure power-law and the jets are relativistic, then systematic variation between the observed spectra of the jet and counterjet are expected. Overall, the SE hotspot has a spectral index flatter than the NW hotspot, and we find no significant correlation between the spectral profiles of the two components over our geometric area of integrated flux density in the present analysis. Since these compact regions of intense radio emission, at least in FR IIs, are sites of AGN jet termination with consequent interaction with the lobe material (or plume material in the case of FR Is) forming strong shocks – to yield physical conditions required for particle acceleration (e.g. Massaglia 2007); it is quite enticing to associate spectral flattening in the hotspots of our sample (which falls at the FR I/FR II break) with such sites of high energy particle acceleration – particularly at the SE hotspot which shows pronounced spectral flattening over almost the entire integration region in the present analysis.

4.3.3 *The plumes*

We used 20 polygon slices each along the plumes for estimating the spectral indices in the large-scale components. The respective profiles are plotted in Figure 7 with their corresponding flux densities and errors. These show a systematic steepening of α in the NW plume compared with the practically constant distribution of α for the SE over the majority of the integration region. However, towards the tail end in both plumes there is an upturn in the spectral index from -1.60 ± 0.01 to -2.26 ± 0.05 ($\Delta\alpha = -0.66$), and -1.37 ± 0.01 to -1.99 ± 0.03 ($\Delta\alpha = -0.62$) for the NW and SE plumes respectively. The overall steepening of the spectra with increasing distance from the sites of particle injection in both plumes is consistent with synchrotron theory; and except for the final 3 locations at the tail end of each spectrum, there is no significant dispersion ($<\delta\alpha> = \pm 0.01$) between the SE and NW plumes. The mean difference between the NW and SE plume is $<\alpha_{NWp} - \alpha_{SEp}> = -0.05 \pm 0.02$. By this measure, the spectral steepening between the two large-scale components is not very significant; consistent with a constant spectral index change for both plumes.

For reasons discussed in section 4.2 above, we have examined the spectral gradients of the NE plume in more detail. We have plotted profiles of spectral index in the plumes in two representations: as unaveraged slices across – (i) the whole plume, and (ii) inner region (which span an angular extent of $\sim$ 61.5 arcsec) to show the level of variation on large and small scales respectively; and to compare α in the dip in this region with respect to the overall plume. The profile is as shown in Figure 7 (top pane). The clear

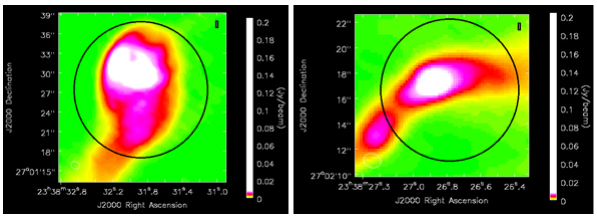

Figure 5. 1.5 GHz VLA maps (A+B–configuration) at 1.4×1.1-arcsec resolution showing the hotspot regions in the WAT source 3C465. Left: SE hotspot. Right: NW hotspot.

tendency for the spectra to flatten slightly within the inner regions of the NW plume is confirmed; with the brightest spot in the region coinciding with comparatively the flattest spectra ($\alpha = -0.938 \pm 0.002$) – indicating the injection of young electron population into the base of the NW plume, and possible acceleration of particles at this site.

In general the spectrum of the NW plume is steeper $<\alpha_{NWp}> = -1.43 \pm 0.01$ compared with the SE $<\alpha_{SEp}> = -1.38 \pm 0.01$, and this is likely the consequence of variations in mass injection and propagation in external pressure and density gradients in the two regions. Conventionally, as the radio jet breaks through the dense ICM and transitions into plumes the spectra will steepen further away from the AGN due to radiative ageing; and this is consistent with our observed spectral behaviour in the two components. It is interesting to note that Figure 7 shows a systematic pattern in the spectral distribution measured in both plumes. The two possibilities to this occurrence are; (1) the correlations result from residual calibration errors, or (2) there exist a similar trend in the spectral index evolution of the two plumes. Given our good image fidelity and robust estimate of the errors in I, we rule out option 1, and argue that both plumes probably have comparable spectral indices over the integration regions in our present analysis. This inference is again consistent with the conclusion that similar flow dynamics is at play in the two components with the observed asymmetry in total intensity a direct consequence of projection effects. Additional evidence for this conclusion can be drawn from the good agreement between the integrated spectral indices measured at the initial 8 locations of the SE plume and the spectral profile of the inner regions of the NW plume. Both show a bell-shaped spectrum within the first few kpc from the edge of the integration region marking the transition from jet to plumes, despite the absence of a distinct continued collimated outflow in the SE plume.

Overall our spectral profiles suggest that the plumes are approximately homologous structures, in the sense that there is a clear trend in their spectral distributions despite evidence of considerable local variations in physical size and structure. While the uncertainties are large near the tail end of the spectrum, there is evidence for a mild trend toward a steeper spectral indices with decreasing flux density in both plumes. We note that the spectral index limits in the respective components originate from the limiting flux density of the least-sensitive frequency (~ 8.5 GHz) in our two-point spectral index calculation.

4.4 Constraints on particle acceleration in 3C465

It is well established that the evolution of radio jets is governed by the balance of particle acceleration and energy-loss processes (e.g. Laing & Bridle 2013). These energy losses affect the overall particle energy distribution in an ensemble of particles, and consequently the resulting synchrotron spectrum. For a power law distribution – i.e., an ensemble of homogeneous and isotropic population of electrons, $N(\varepsilon, 0)\, d\varepsilon = N_\circ \varepsilon^{-\delta}$; there exists a corresponding power law synchrotron spectrum, $S(\nu) \propto \nu^{\alpha}$, the logarithmic slope of which relates the Mach number of the accelerating shock. For a detailed account on the subject, see Hardcastle (2013) and references therein. The case of astrophysical interest from standard model in which relativistic electrons suffer radiative and adiabatic losses as the radio jet propagate, is consistent with the spectral steepening we observe, away from the AGN. We note that relatively high frequency (~ 8.5 GHz) emission observed at large distances from the hotspots implies plausible *in situ* acceleration of relativistic particles in *at least* some parts of the extended structures. This again agrees with the observed spectral flattening at a few discrete locations in both plumes as seen in our spectral profile plots.

A good assessment of possible jet particle acceleration mechanisms is provided elsewhere (e.g. Heavens 1984; Bisnovatyi-Kogan & Lovelace 1995; Rieger et al. 2007; Summerlin & Baring 2012; Liu et al. 2017). Fermi acceleration is the most popular scheme; with first-order Fermi acceleration thought to be the main particle acceleration mechanism at collisionless MHD shocks (e.g. Laing & Bridle 2013). Other acceleration mechanisms, the so called "second order" processes are generally thought to be less efficient, but as pointed out by Ostrowski & Schlickeiser (1993), the gradient of the relativistic particles in all cases approaches a power law at lower frequencies that reflects the acceleration physics. It has long been established that particle acceleration process that sets the *energy spectrum* does not occur in the *extended lobes* (plumes) of extragalactic radio sources (e.g. Hughes 1980). Plumes are normally assumed to be just passive outflows, and although wave generation within the plume material may allow particle acceleration there, the fact that we observe the spectra to steepen monotonically as you go away from the hotspots does not provide any such evidence. This notwithstanding, in the present study, we posit that acceleration if occurring at all would be more likely distributed throughout the plumes of 3C465, rather than restricted to a few localised sites containing peak brightness, and that the observed variation in spectral profiles results from the combined effects of synchrotron and adiabatic (energy transferred to surrounding medium only as work) losses, in addition to the underlying acceleration mechanism, as per discussions below.

i. Non-relativistic shocks

Contrary to earlier work (e.g. Bell 1978) in test particle diffusive shock acceleration (test particle approximation), recent work (e.g. Laing & Bridle 2013) have established that steeper spectra can in principle be produced in weaker, non-relativistic shocks. Since our velocity estimate implies that the jet in 3C465 is mildly relativistic at the base, it is appropriate to assume non-relativistic flows/speeds in the extended structures due to deceleration resulting from entrainment by ambient material. Thus, the observed spectral steepening in the plumes is more likely the result of weak, non-relativistic shocks in the plume material.

ii. Mildly relativistic shocks

Previous studies (e.g. Summerlin & Baring 2012) have shown that, depending on the nature of scattering, shock speed and field obliquity, mildly relativistic shocks can generate a wide range of power law slopes for the energy spectrum. Our observations indicate mildly relativistic speeds in the jet (at least in the inner regions close to the core) and thus require energy indices that depends on mean flow speed. Mildly relativistic speed upstream of the shock front

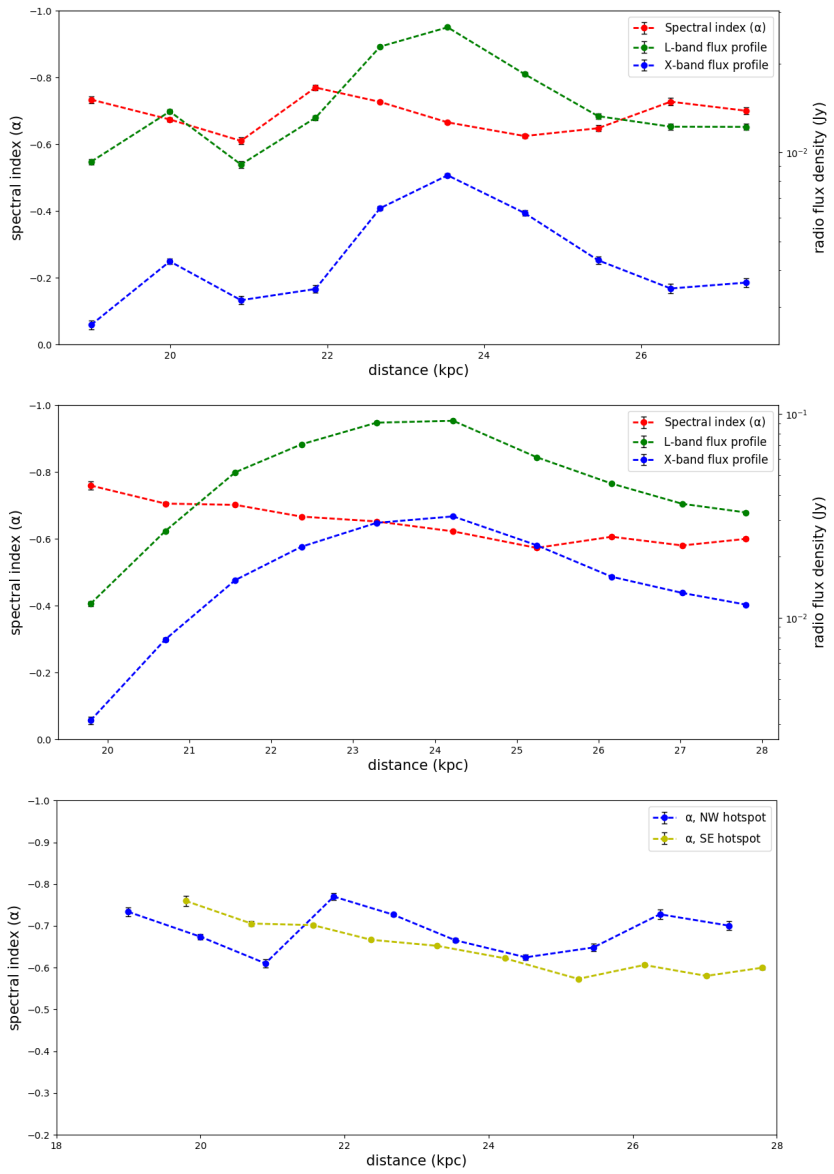

Figure 6. Distribution of spectral indices, $\alpha_{1.5}^{8.5}$ for the two hotspot regions plotted as a function of distance from the nucleus. Also shown are the respective flux density distributions. Top: NW hotspot. Middle: SE hotspot. Bottom: Composite plot of the two components. The spectral indices were calculated from total intensity integrated over a circle of diameter 16.05 arcsec centred on the two components; and error bars as in Figure 17.

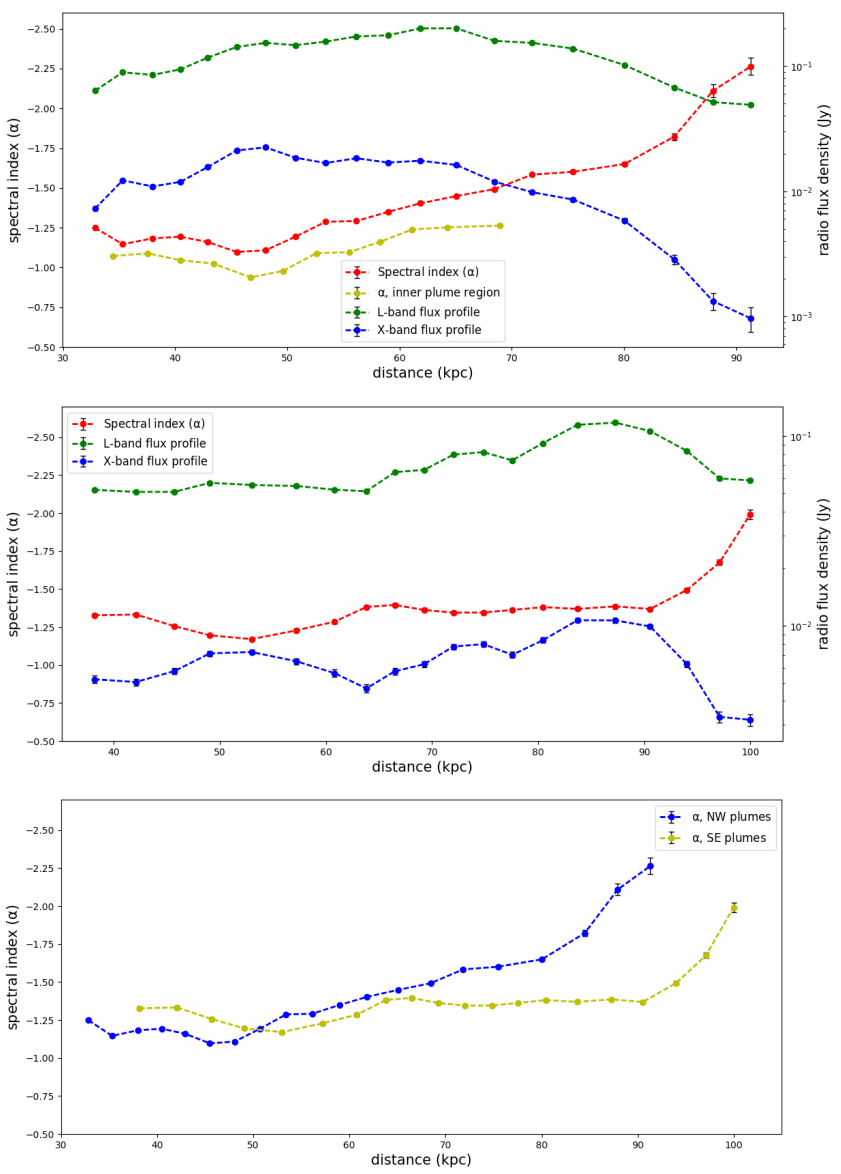

Figure 7. Variation in spectral indices $\alpha_{1.5}^{8.5}$ with fiducial distance in the extended structures of 3C465. Top: NW plume; also shown here is a profile of the continued collimated outflow at the base of the NW plume as seen in total intensity (Fig. 14). Middle: SE plume. Bottom: composite plot of the two components. Estimate of α and corresponding errors are as quoted in Fig. 17.

seems the most likely scheme which meets this requirement. Thus, we argue that the observed synchrotron spectra in the jet of 3C465, and more so the spectral flattening in the inner regions close to the core (where the bright knots form), results from mildly relativistic shocks. We find our result to be consistent with earlier work by Laing & Bridle (2013) in which they suggested that mildly relativistic shocks are responsible for the range of physical conditions in FR I jet bases.

iii. Ultra-relativistic shocks

For outflows containing considerable amounts of non-relativistic protons entrained by ambient material, Laing & Bridle (2002) suggest that the sound speed, β_s may be significantly lower than the lower limit of 0.58 in the jet for an ultra-relativistic plasma, and may vary systematically with position in the jet. From our inferred mean value, $<\alpha_{jet}> = -0.70 \pm 0.04$, it is plausible that the jet composition in our sample is dominated by ultra-relativistic particles and magnetic field, and may be considerably higher or lower than this asymptotic value wherever the average flow speed is even slightly supersonic or transonic respectively.

Numerical (e.g. Ellison & Double 2004) and analytical (e.g. Kirk et al. 2000) results have also shown that ultra-relativistic shocks in principle can produce a power law energy spectrum with $\delta = 2.23$ ($\alpha = 0.62$). Comparison with our observed mean α values of -0.69 ± 0.01 (-0.65 ± 0.01) for the NW and SE hotspots respectively suggests that both components have marginally but significantly steeper spectral indices than predictions from theory. Given this discrepancy and our constraints on the jet speed ($\beta_s \geq 0.5$), it seems rather unlikely that ultra-relativistic shocks are relevant to the physical conditions of these compact regions of intense radio emission. However, in the absence of independent statistical evidence, it is plausible that the flow at the hotspots is supersonic everywhere, suggesting strong "*relativistic*" shocks in this flow regime that can be modified by back-pressure of the accelerated cosmic rays. This in principle would alter the shape of the synchrotron spectrum as seen in our respective hotspots spectral profiles.

4.4.1 *Acceleration mechanisms*

Our analysis shows that first-order Fermi processes at mildly relativistic shocks are the most probable acceleration mechanism at play in 3C465 – evident in the observed synchrotron spectrum along the jet axis. Laing & Bridle (2013) suggest that a likely complication may exist, in the sense that, X-ray particle acceleration requires a distributed system of shocks covering a significant distance along the jet axis rather than restricted to a few localized shock sites. In the present study, such shock systems can be associated with the multiple bright knotty structures at the jet base (Fig. 2(d)), as well as the complex, non-axisymmetric brightness structure of the two hotspot regions (Fig. 5).

Since we infer mildly relativistic flow in our radio sample, we argue that two distinct acceleration mechanisms exists at the base of the radio jet.

1. The first mechanism is governed by flow speeds, $\beta_j \geq 0.5$, and seems the likely dominant acceleration process in the jet base – inferred from our lower limit of 0.5 for β_j. Since knots and hotspots are approximately homologous structures, it is plausible, particularly in the high-emissivity regimes (hotspots) for strong relativistic shocks to occur. These shocks have the tendency to accelerate electrons to high Lorentz factors, allowing X-ray synchrotron emission in the hotspot regions comparable to that observed by Hardcastle et al. (2005) in the bright knots at the jet base.

2. The second mechanism dominates wherever the flow speed, β_j falls below ≈ 0.5. In this regime, there is deceleration by entrainment such that the flow is transonic and dominated by weaker shocks. As pointed out by Rieger & Duffy (2004), steady shear acceleration bracket this condition, and implies that transverse velocity gradients must exist in these regions. In addition to the jet base, we favour this scheme as the likely dominant process at play in the extended structures (radio plumes) of our sample, particularly as β_j approaches a limiting value ($\ll 0.5$) – implying non-relativistic flows/shocks in this regime.

We infer evidence for particle acceleration in the plumes based on the observed continued collimated outflow of plasma from the site of particle injection (hotspots) into the plume materials. This compare with predictions from twin-beam model for radio sources (e.g. Blandford & Rees 1974), and as noted by Blandford & Eichler (1987), these high energy electron population, which are responsible for emission at such large distances must have been accelerated *in situ*, most likely via weaker/non-relativistic shock acceleration as seen in the present study. We note here that, it is still not clear whether or not there is any *real* acceleration in this "flow regime" or whether the spectral structures we see are just the result of newly accelerated particles mixing with the old ones in the plume material.

Overall, we infer two different acceleration mechanisms at the base of the radio jet in our sample, consistent with previous high resolution multi-waveband (radio to X-ray) studies of FR I jet bases (e.g. Hardcastle et al. 2003; Perlman et al. 2011). These two mechanisms similarly account for the acceleration process in the hotspots and plumes, although in the case of the hotspots, there is a slight tendency that the required speed will be significantly higher than our estimated value of $0.5c$ in the present analysis. The systematic difference in the observed spectral profiles for the three regions (jet, hotspots and plumes) relates these distinct mechanisms. We note that by this conclusion, we are by no means neglecting the likelihood of second-order Fermi acceleration as possible alternative mechanism.

5 CONCLUSION AND FUTURE WORK

We have presented the highest resolution and sensitivity maps to date of the WAT source 3C465 jet, derived by combining radio data from e-MERLIN and VLA observations. Total intensity maps and a spectral index map (derived from two frequencies at 1.5 arcsec resolution) of the source are also presented. A comprehensive description of these maps and detailed spectral analysis to study the plausible underlying mechanisms of where and how particles are accelerated in the jet, knots, hotspots and plumes of the radio source have also been presented.

We obtain a sidedness ratio of 14.85 ± 0.80 and consequently derive lower and upper limit values of $0.5c$ and 61° for the jet speed, β_j and angle to the line of sight, θ respectively. The principal results from our detailed study of the spectral index distribution are as follows:

(i) The spectral profile is fairly constant over almost the entire jet length with a mean value of, $<\alpha_{jet}> = -0.7 \pm 0.04$, as expected from radio synchrotron emission.

(ii) The spectral flattening within the first 4.42 kpc radius from the core coincides with the region hosting the bright knots, and is

consistent with the site of X-ray particle acceleration at the base of the radio jet observed by Hardcastle et al. (2005).

(iii) The spectral indices in the hotspot regions show very little dispersion between the two components with mean values of $<\alpha_{NWh}> = -0.69 \pm 0.01$ and $<\alpha_{SEh}> = -0.65 \pm 0.01$ ($<\Delta\alpha> = -0.04$), indicating plausibly electron population of the same properties is injected at these sites.

(iv) Our spectral profiles suggest that the plumes are approximately homologous structures, in the sense that there is a clear trend in their spectral distributions despite evidence of considerable local variations in physical size and shape. We associate this asymmetry in morphology to variations in mass injection and propagation in external pressure and density gradients in the two regions, and this accounts for the comparatively steeper spectrum in the NW plume, $<\alpha_{NWp}> = -1.43 \pm 0.01$ compared with the SE plume, $<\alpha_{SEp}> = -1.38 \pm 0.01$. There is also a clear tendency for the spectra to flatten slightly within the inner regions of the NW plume – indicating the injection of young electron population into the base of the NW plume, and plausible acceleration of particles at this site.

(v) First-order Fermi process at mildly relativistic shocks is the most probable acceleration mechanism at play in the radio source 3C465. Consistent with earlier work by Laing & Bridle (2013), we infer two acceleration mechanisms; (a) when bulk flow speeds, $\beta_j \geq 0.5$, and (b) when flow speeds, β_j are less than ≈ 0.5. The first case can accelerate electrons to high Lorentz factors, whereas the second scenario must occur at slower speeds and larger distances.

For future work, we aim to observe over a broad range of frequencies to study in detail the *deviations from power law spectra* which are indicators of synchrotron ageing and plausible diagnostics of the acceleration mechanism and as well, investigate the orientation and degree of ordering of magnetic field in the jet base.

ACKNOWLEDGEMENTS

This research was undertaken with a studentship through the Development in Africa with Radio Astronomy (DARA) project funded by the UK's Newton Fund. EBM would like to thank Javier Moldon (e-MERLIN Project Scientist) for assisting in the initial data reduction process of the e-MERLIN data at Jodrell Bank Centre for Astrophysics, University of Manchester.

The National Radio Astronomy Observatory is a facility of the National Science Foundation operated under cooperative agreement by Associated Universities, Inc. The e-MERLIN is UK's national facility for radio astronomy and is operated by the University of Manchester from the Jodrell Bank Observatory (JBO) on behalf of the Science and Technology Facilities Council (STFC).

This work has made use of the University of Hertfordshire's high-performance computing facility (`https://uhhpc.herts.ac.uk/`).

REFERENCES

Bell A. R., 1978, MNRAS, 182, 147
Biggs A. D., Ivison R. J., 2008, MNRAS, 385, 893
Bisnovatyi-Kogan G. S., Lovelace R. V. E., 1995, A&A, 296, L17
Blandford R., Eichler D., 1987, Phys. Rep., 154, 1
Blandford R. D., Rees M. J., 1974, MNRAS, 169, 395
Bodo G., Ferrari A., Massaglia S., Tsinganos K., 1985, A&A, 149, 246
Burns J. O., Eilek J. A., Owen F. N., 1982, in Heeschen D. S., Wade C. M., eds, IAU Symposium Vol. 97, Extragalactic Radio Sources. p. 45
Capetti A., Verdoes Kleijn G., Chiaberge M., 2005, A&A, 439, 935
Colina L., Perez-Fournon I., 1990, ApJS, 72, 41
Eilek J. A., Burns J. O., O'Dea C. P., Owen F. N., 1984, ApJ, 278, 37
Ellison D. C., Double G. P., 2004, Astroparticle Physics, 22, 323
Fanaroff, B. L. and Riley, J. M., 1974, MNRAS, 167, 31P
Hardcastle M. J., 1998, MNRAS, 298, 569
Hardcastle M. J., 2013, MNRAS, 433, 3364
Hardcastle M. J., Sakelliou I., 2004, MNRAS, 349, 560
Hardcastle M. J., Alexander P., Pooley G. G., Riley J. M., 1998, MNRAS, 296, 445
Hardcastle M. J., Worrall D. M., Birkinshaw M., Laing R. A., Bridle A. H., 2002, MNRAS, 334, 182
Hardcastle M. J., Worrall D. M., Kraft R. P., Forman W. R., Jones C., Murray S. S., 2003, ApJ, 593, 169
Hardcastle M. J., Sakelliou I., Worrall D. M., 2005, Mon. Not. Roy. Astron. Soc., 359, 1007
Heavens A. F., 1984, MNRAS, 210, 813
Hughes P. A., 1980, MNRAS, 193, 277
Jetha N. N., Hardcastle M. J., Sakelliou I., 2006, MNRAS, 368, 609
Kirk J. G., Guthmann A. W., Gallant Y. A., Achterberg A., 2000, ApJ, 542, 235
Laing R. A., 1993, in Davis R. J., Booth R. S., eds, Sub-arcsecond Radio Astronomy. p. 346
Laing R. A., Bridle A. H., 2002, MNRAS, 336, 1161
Laing R. A., Bridle A. H., 2013, MNRAS, 432, 1114
Laing R. A., Canvin J. R., Cotton W. D., Bridle A. H., 2006, MNRAS, 368, 48
Leahy J. P., 1984, MNRAS, 208, 323
Leahy J. P., Bridle A. H., Strom R. G., 1996, in Ekers R. D., Fanti C., Padrielli L., eds, IAU Symposium Vol. 175, Extragalactic Radio Sources. p. 157
Liu R.-Y., Rieger F. M., Aharonian F. A., 2017, ApJ, 842, 39
Massaglia S., 2007, Nuclear Physics B Proceedings Supplements, 168, 302
O'Donoghue A. A., Eilek J. A., Owen F. N., 1993, ApJ, 408, 428
Offringa A. R., et al., 2014, MNRAS, 444, 606
Oort M. J. A., Windhorst R. A., 1985, A&A, 145, 405
Ostrowski M., Schlickeiser R., 1993, A&A, 268, 812
Owen F., Rudnick L., 1976, ApJ, 205, L1
Parma P., de Ruiter H. R., Mack K.-H., van Breugel W., Dey A., Fanti R., Klein U., 1996, A&A, 311, 49
Perlman E. S., et al., 2011, ApJ, 739, 65
Rieger F. M., Duffy P., 2004, ApJ, 617, 155
Rieger F. M., Bosch-Ramon V., Duffy P., 2007, Ap&SS, 309, 119
Scheuer P. A. G., Readhead A. C. S., 1979, Nature, 277, 182
Schindler S., Prieto M. A., 1997, A&A, 327, 37
Stone J. M., 1997, in Reipurth B., Bertout C., eds, IAU Symposium Vol. 182, Herbig-Haro Flows and the Birth of Stars. pp 323–333
Summerlin E. J., Baring M. G., 2012, ApJ, 745, 63
Urry C. M., Padovani P., 1995, PASP, 107, 803
Venkatesan T. C. A., Batuski D. J., Hanisch R. J., Burns J. O., 1994, ApJ, 436, 67
Wiita P. J., 2001, ArXiv Astrophysics e-prints,
Worrall D. M., Birkinshaw M., Cameron R. A., 1995, ApJ, 449, 93
Worrall D. M., Birkinshaw M., Kraft R. P., Hardcastle M. J., 2007, ApJ, 658, L79

This paper has been typeset from a TEX/LATEX file prepared by the author.